Time-resolved Light Transport Decomposition for Thermal Photometric Stereo

Kenichiro Tanaka   Nobuhiro Ikeya   Tsuyoshi Takatani
Hiroyuki Kubo   Takuya Funatomi   Yasuhiro Mukaigawa

Nara Institute of Science and Technology (NAIST), Japan

{ktanaka, ikeya.nobuhiro.ii6, takatani.tsuyoshi.to2, hkubo, funatomi, mukaigawa}@is.naist.jp

Abstract

We present a novel time-resolved light transport decomposition method using thermal imaging. Because the speed of heat propagation is much slower than the speed of light propagation, transient transport of far infrared light can be observed at a video frame rate. A key observation is that the thermal image looks similar to the visible light image in an appropriately controlled environment. This implies that conventional computer vision techniques can be straightforwardly applied to the thermal image. We show that the diffuse component in the thermal image can be separated and, therefore, the surface normals of objects can be estimated by the Lambertian photometric stereo. The effectiveness of our method is evaluated by conducting real-world experiments, and its applicability to black body, transparent, and translucent objects is shown.

1. Introduction

Light transport decomposition has attracted broad interest in the computer vision and computer graphics fields. This is because many computer vision techniques implicitly or explicitly assume only diffuse reflection, which simplifies observation models. An image in the real world is, however, composed of many optical components, such as specular reflection, inter-reflection, and subsurface scattering. Light transport decomposition plays an important role to bridge the gap between the real world and the models.

Prior works have decomposed light transport using color [41], polarization [47], and active illumination [29]. The time-resolved approach has emerged because the each optical components has different transient properties on the tens of pico seconds order [52]. There are multiple time-resolved approaches, for example, with the use of a femto-pulsed laser, interferometer [6], time-of-flight camera modifications [10, 20], and single-photon sensor [36]. Inspired by the temporal decomposition of light transport, we develop a novel time-resolved decomposition technique for

(a) A ball.   (b) Color image.   (c) Thermal image.

Figure 1: A ball captured by a conventional color camera and a thermal camera. (a) The target object. (b) Reflection image using a conventional camera. (c) Thermal image of the same object. When the object is carefully illuminated, shading of both images is the same, which implies conventional computer vision techniques can be applied to the thermal images.

far infrared light transport. A key observation is that the speed of heat propagation is extremely slow compared with the speed of light propagation. Using thermal imaging, the time-resolved decomposition is feasible at a video frame rate.

To date, thermal imaging has been treated as being different from visible light imaging: The thermal image represents the temperature of the object, while the visible light image reflects the visual information. We show, however, similar images can be obtained when the observation environment is appropriately controlled, because thermal imaging makes up a part of far infrared light imaging. Figure 1 shows an image captured by a color camera and a thermal image, where a ball is illuminated by a point light source. Both the color image and the thermal image exhibit the same shading. This observation implies that computer vision techniques can also be applied for thermal images.

In this paper, we show that far infrared light transport can be regarded as a composition of multiple optical and thermal effects similar to the visible light transport. We define ambient, specular, diffuse, and global components in the thermal observation, and show the transient property of each component. Based on this model, a time-resolved de-

composition of the far infrared light transport is proposed. Moreover, we show that the surface normal can be estimated based on the Lambertian photometric stereo, because the diffuse component, which follows the cosine law, of the far infrared light is separated. The proposed thermal photometric stereo can be applied for any objects that absorb light and convert it into heat, including black body, transparent, and translucent objects. It has a wide applicability compared with the photometric stereo using visible light.

The chief contributions of this study are threefold. First, we extend the visible light transport model to the far infrared light transport. We show that the thermal image is a composition of ambient, specular, diffuse, and global components, which is similar to the visible light transport. Second, a novel approach for time-resolved light transport decomposition is provided based on the difference of the transient property of the far infrared light transport. Finally, we show that ordinary computer vision techniques can be straightforwardly applied to thermal images. As a proof of the concept, we propose a method to recover the surface normal using a photometric stereo after decomposing the far infrared light transport. The surface normal of challenging objects that have complicated optical effects can be recovered.

2. Related Work

Light transport decomposition Light transport decomposition is a key technology for computer vision and graphics because many techniques are based on the simple reflection model. The decomposition research started from a color-based approach. Shafer *et al*. [41] propose the dichromatic reflectance model, in which specular reflection depends on the color of the light source while diffuse reflection depends on the color of the object. Many works employ this model to separate the diffuse and specular reflections [40, 31, 38]. Using polarizers is another approach to separate light transport. Wolff and Boult [50] separate diffuse and specular reflections using linear polarization. Diffuse reflection and volumetric scattering can also be separated using circular polarization [47]. Active illumination is an effective approach to decompose light transport. Nayar *et al*. [29] separate direct and indirect reflections using high-frequency pattern projection. Many extensions are proposed to separate specular and diffuse reflections [21], transmission and scattering [45], and single scattering and multiple scattering [24]. O'Toole *et al*. [35, 34, 32] decompose light transport using an epipolar constraint. Our far infrared light transport decomposition falls into this type of research, although this is the first work on far infrared light transport decomposition.

Time-resolved decomposition of light transport is an emerging technology to separate the light transport components. Wu *et al*. [52] develop a method to decompose diffuse reflection, inter-reflection, and subsurface scattering based on the temporal response of a femtosecond-pulsed laser. Resolving the multi-path problem in the time-of-flight camera is an active research topic and it has been studied by assuming the two-bounce or simplified reflection models [5, 2, 7, 16], K-sparsity [1, 4, 37], parametric model [12, 19], consistency between ToF and stereo [22], simplified indirect reflections [26], and large-scale multi-path [17]. It can be used to measure a slice of BRDF [27], perform non-line-of-sight imaging [11, 18, 48], and recover the shape of transparent and translucent objects [42, 43]. Direct and indirect light transport can also be decomposed by the time-resolved approach [52, 33, 8, 6]. While these methods are effective, they require sub-nanosecond operations and are not easy to perform for many people. Inspired by these methods, we propose a novel time-resolved approach using thermal imaging. Because the time scale of the heat propagation is a million times slower than that of light, time-resolved light transport decomposition can be achieved at a video rate.

Shape recovery The photometric stereo has been a broad interest in the computer vision field. The Lambertian photometric stereo [51] is a standard way to recover the surface normal by assuming Lambert reflection, no optical effect such as shadow and scattering, orthogonal projection, and parallel lights. To apply the Lambertian photometric stereo for a non-Lambert surface, other optical components need to be separated by pattern projection [29], polarization [28], and fluorescence [46]. Similar to these approaches, we apply the Lambertian photometric stereo after extracting the diffuse component.

Inoshita *et al*. [14] improves the photometric stereo for translucent objects using surface normal deconvolution, Ngo *et al*. [30] use a polarization cue to recover a smooth surface, and Murez *et al*. [25] develop a photometric stereo in a scattering media that consider the blur depending on the distance. While these methods jointly compensate for the global light transport in their solutions, we aim to separate the far infrared light transport.

There is a small number of thermal imaging approaches to solve computer vision problems. Saponaro *et al*. [39] estimate the material from the water permeation and heating/cooling process of the object. Miyazaki *et al*. [23] resolve the ambiguity regarding polarization-based shape reconstruction using a thermal image. Eren *et al*. [3] recover the transparent shape by triangulation using laser beam spot heating and thermal imaging. We are interested in the decomposition of far infrared light transport so that the surface normal can be simply recovered by the Lambertian photometric stereo.
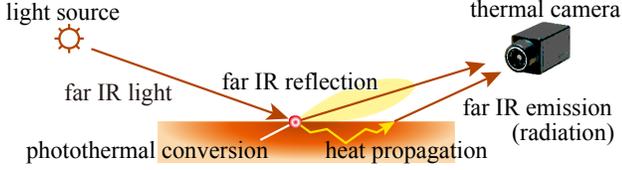
Figure 2: Far infrared light transport. While far infrared light can partially be reflected on the surface, the rest of the light is converted to heat energy, propagates inside the object, and is then converted to far infrared light corresponding to the temperature. The composition of all the components are captured by a camera. The observation system is closed in the far infrared light domain.

3. Far infrared light transport

We start with a brief review of thermal and far infrared light imaging. A typical thermal camera observes the temperature of the object by measuring the intensity of far infrared light because all objects emit far infrared light according to its temperature. When the object is a black body, the temperature and the intensity of far infrared light are governed by the Stefan-Boltzmann law [13], which represents a one-to-one correspondence between temperature and intensity:

$$E = \sigma T^4, \tag{1}$$

where E is the intensity of the radiated far infrared light, σ is the Stefan-Boltzmann constant, and T is the thermodynamic temperature. We can handle the intensity of the far infrared light as the temperature, and vice versa.

We assume that the scene is illuminated by a stable parallel light source of far infrared light and the object is captured by a thermal camera as shown in Fig. 2. When the object is not a black body, a part of the far infrared light reflects on the surface, while the rest of the light is absorbed and converted to the heat energy, the temperature increases, and far infrared light is emitted corresponding to its temperature. The observation is the sum of these effects and we term this total energy transport as *far infrared light transport* because the observation system is closed in the far infrared light domain.

An image captured by a normal camera is the composition of multiple light transport effects, *e.g.*, specular and diffuse reflections, inter-reflection, and subsurface scattering. Similarly, the thermal image is a sum of the multiple far infrared light transports as shown in Fig. 3. A main difference between visible and far infrared light transport is that the temporal transient properties are significantly different among the light transport components. The transient state of visible light transport is not observable at a video frame rate because the speed of light is extremely fast, while that of the far infrared light transport is easily observable

because the heat conversion and propagation are relatively slow. Figure 4 illustrates a concept of the temperature transition of the far infrared light transport components. Before the light source is turned on, the observation consists of only the ambient component. The specular reflection appears immediately after the light source is turned on, and diffuse and global radiation slowly appear as the temperature increases. Then, the diffuse radiation reaches the steady state faster than the global radiation.

The observed thermal image $I(t)$ at a video frame t can be modeled as

$$I(t) = A(t) + S(t) + D(t) + G(t), \tag{2}$$

where A, S, D, G are the ambient, specular reflection, diffuse radiation, and global radiation components, respectively. We omit the camera pixel c because this observation is pixel-wise, and we assume the light source is turned on at $t = 0$ without the loss of generality. We review the detailed properties of the far infrared light transport components below.

Ambient The ambient component is the original temperature of the object. This corresponds to the intensity of far infrared light coming from the object when the heat source is turned off. The ambient component is assumed to be constant over time, and the effect of the heat source can be extracted by subtracting the initial state of the heat radiation. In the context of optical measurements, the ambient component corresponds to the ambient light or the dark current. The ambient component $A(t)$ is expressed as

$$A(t) = \tau, \tag{3}$$

where τ is the original temperature of the object.

Specular reflection The specular component is an effect of far infrared light itself and not related to the heat propagation or temperature of the object. In the temperature measurement context, the specular component disturbs the observed temperature. Because it is the behavior of light, the specular component has the same properties as the visible light transport. The specular component $S(t)$ is only observed when the light source is turned on as

$$S(t) = \begin{cases} L_0 r_S & (t > 0) \\ 0 & (t \leq 0) \end{cases}, \tag{4}$$

where r_S is the specular reflectance, and L_0 is the intensity of the ideal light source. Because the speed of light is very fast, the specular component is stable and no transient state is observed on the video frame scale. Note that we ignore other optical effects such as diffuse reflection and subsurface scattering because they can be negligible for many

(a) Ambient (b) Specular reflection (c) Diffuse radiation (d) Global radiation
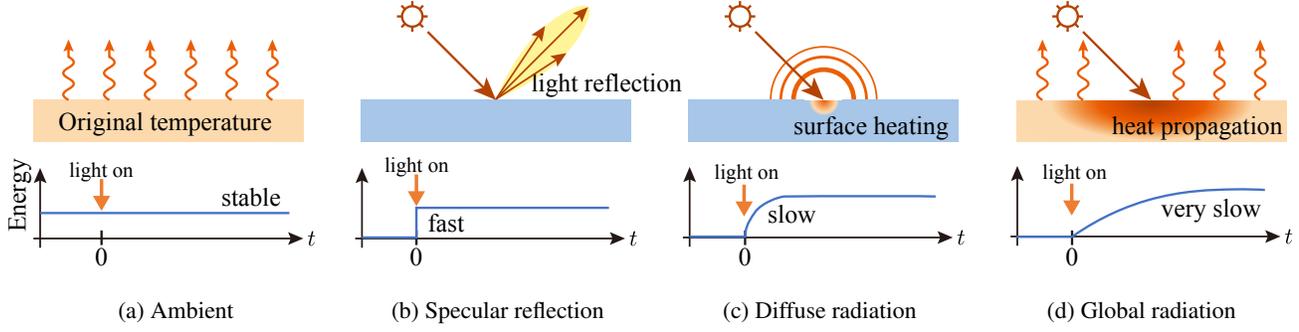
Figure 3: Far infrared light and heat transport components. Similar to the visible light transport, far infrared light transport consists of (a) ambient, which is the original temperature, (b) specular reflection as light, (c) diffuse radiation, and (d) global radiation caused by heat propagation. Because the speed of heat is slower than that of light, every components has distinctive transient properties hence they are separable.
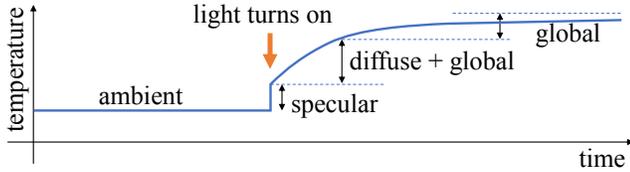
Figure 4: Transient properties of far infrared light transport. Because the temporal responses of the components are significantly different, they can be separated from the thermal video frames.

materials owing to the long wavelength. They have however the same transient property, hence they can be safely regarded as a part of the specular reflection.

Diffuse and global radiation Diffuse radiation is defined as the surface heating. The energy is absorbed on the surface and the temperature of the surface is raised by photothermal conversion. Corresponding to the irradiance of light, the absorption energy of the incident far infrared light follows the cosine law [13]. The emission energy is linear to the absorbed energy, which is known as Kirchhoff's law of thermal radiation [13], which is given as

$$\alpha E = \varepsilon E, \tag{5}$$

where α and ε are the coefficients of absorption and emission, respectively. The raised temperature can be observed from any camera position; hence it corresponds to the Lambertian reflection of visible light transport. Because diffuse radiation is the effect on a single point, it is nearly stable but there is a small transient state when the energy is absorbed, the temperature is raised, and far infrared light is emitted. Compared with the temporal spread of diffuse reflection [49], which is about tens of picoseconds, the temporal scale of diffuse radiation is much slower, and can be

captured at the video frame rate.

When the object is heated over a sufficiently long time, the temperature is propagated in all directions, and we term this heat propagation as *global radiation*. Heat propagation is very slow, where it takes a few seconds to minutes, which is much slower than the diffuse radiation. Because global radiation spreads spatially, it corresponds to the subsurface scattering in the visible light observation.

Because the intensity of the far infrared light corresponding to the inner temperature follows the Fresnel law [23], the global radiation varies with respect to the viewing angle. However, it works as a scale factor with our setting, hence the effect of Fresnel refraction can be safely ignored.

It has been reported that the diffuse reflection and subsurface scattering can be regarded as the same physical phenomenon [15, 9, 44]; the light scatters on or beneath the surface and eventually bounces off of the material in random directions. Diffuse reflection represents the total intensity of light close to the incident point on the surface, and the subsurface scattering represents the light at a distance away from the incident point on the surface. The same thing can be said of the radiation; diffuse radiation is the heat energy whose heating point is local and global radiation is the heat that is propagated in all directions. Separating these components is a heuristic problem and we adopt exponential fitting to separate them.

We model the transient state of radiation using the exponential functions as

$$\begin{cases} D(t) & = R_\infty(1 - e^{-\sigma_d t})d_\infty \\ G(t) & = R_\infty(1 - e^{-\sigma_g t})g_\infty, \end{cases} \tag{6}$$

where σ_d and σ_g ($\sigma_g \ll \sigma_d$) represent the coefficient of the transient speed of diffuse and global radiations, respectively, and d_∞ and g_∞ represents the ratio of diffuse and the global radiation components at the steady state to the total radiation, respectively.

4. Thermal Photometric Stereo

Based on the difference in the transient properties of the far infrared light transport components, we develop a decomposition method and thermal photometric stereo.

4.1. Decomposition

Based on the observation of the transient properties, we decompose these components. First, the ambient component is observed before the light source is turned on. The light source is turned on at $t = 0$, and the specular component is the increased observation immediately after the light source is turned on. The radiation component is the transient state of increasing temperature and it is observed until the temperature becomes steady. Finally, the radiation is separated into diffuse and global radiations based on the speed to reach the steady state. We will next explain the details of the separation.

Separating ambient component The ambient component is the observation before the light source is turned on, and is determined as

$$A = I(0). \tag{7}$$

The transient observation $T_r(t)$ is the rest of the observation, given as

$$T_r(t) = I(t) - A. \tag{8}$$

Separating specular reflection and radiation The specular component is the reflection of light and has no transient state; hence it can be obtained as the increase immediately after the light source is turned on. The specular component S is obtained as

$$S = T_r(\epsilon), \tag{9}$$

where ϵ is an infinitesimal time duration.

The rest is the radiation, which has a temporal transient state. The radiation $R(t)$ can be obtained as

$$R(t) = T_r(t) - S. \tag{10}$$

Separating diffuse and global radiation We fit the radiation components $R(t)$ to the model defined in Eq. (6) as

$$\hat{\sigma_d}, \hat{d_\infty}, \hat{\sigma_g}, \hat{g_\infty} = \underset{\sigma_d, d_\infty, \sigma_g, g_\infty}{\mathrm{argmin}} \; \|R(t) - D(t) - G(t)\|_2^2$$

$$\text{s.t.} \quad \min_t \frac{-\log(R_\infty - R(t))}{t} \leq \sigma_g \ll \sigma_d$$

$$0 \leq d_\infty \leq 1$$

$$0 \leq g_\infty \leq 1$$

$$d_\infty + g_\infty = 1, \tag{11}$$
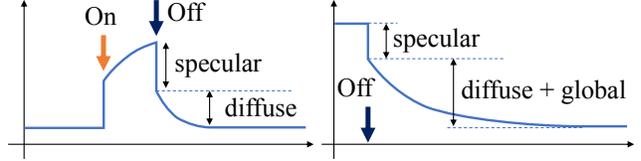
(a) Heating in a short duration.   (b) Transient state of cooling.

Figure 5: Other viable approaches. (a) By turning on and off the light source in a sufficiently short time, the specular reflection and diffuse radiation can be directly obtained. (b) Transient state after the light source is turned off contains similar information.

where $R_\infty = R(\infty)$ is the steady state of the radiation components. The first constraint represents that the time duration to the steady state of each component is smaller than the time for the observation to reach the steady state. Because the diffuse radiation is faster than the global radiation, σ_g is less than σ_d. The second and third constraints represent that the intensity of the diffuse and global radiations are smaller than the total radiation. The last constraint represents that the total radiation is a sum of diffuse and specular reflection, which reduces one degree of freedom. Fitting these parameters is not a convex problem so we use a grid search to find the global optimum. This does not involve a large computational cost because there are only three variables and the boundaries of the parameters can be predicted by the radiation profile $R(t)$.

Other options Another viable approach is to use the decrease in temperature after the light source is turned off. By switching on and off the light source over a short duration, the specular reflection and diffuse radiation can be directly obtained, as shown in Fig. 5(a), because the effect of heat propagation is negligible over a very short time. However, the diffuse radiation does not reach the steady state, hence it may suffer from extremely low SNR. To extend the heating time could improve the SNR, however, the global radiation cannot be ignored. To determine the suitable heating duration is another heuristic problem.

The cooling process is also useful to analyze far infrared light transport as shown in Fig. 5(b). Because heating and cooling are the reverse phenomena, light transport decomposition can be achieved in a very similar way. Because this takes twice as long time, we chose to analyze only the heating process.

4.2. Surface normal estimation

When the object is heated by a narrow beam, the point absorbs the energy and radiates far infrared light according to the increased temperature. The absorbed energy follows

the cosine law [13] as is observed for the light irradiance. Therefore, the diffuse component at the stable state can be represented as

$$D(\infty) = R_\infty d_\infty = R_\infty \rho \mathbf{i}^\top \mathbf{n}, \qquad (12)$$

where ρ is the albedo of heat energy, and $\mathbf{i} \in \mathbb{R}^3$ and $\mathbf{n} \in \mathbb{R}^3$ represent the light direction and surface normal, respectively.

Because the diffuse radiation and diffuse reflection follow the same cosine law, the ordinary photometric stereo can be applied for diffuse radiation. The ordinary photometric stereo is not applicable for black body, transparent objects, and translucent objects that does not have diffuse reflection or are governed by other light transports. However, the diffuse radiation is a phenomenon of energy absorption and emission, so the surface normal of much more objects can be uniformly obtained using diffuse radiation. We propose a photometric stereo approach to the diffuse radiation, which we call the *thermal photometric stereo*.

As shown in Eq. (12), the decomposed diffuse radiation follows the cosine law hence it can be directly used for the Lambertian photometric stereo. The estimated diffuse radiation component $\hat{d_\infty}$ can be simply represented as

$$\hat{d_\infty} = \rho \mathbf{i}^\top \mathbf{n}. \qquad (13)$$

When multiple light sources are placed at different positions, multiple observations can be obtained that can be superposed in a matrix form as

$$\mathbf{d} = \rho \mathbf{I} \mathbf{n}, \qquad (14)$$

where $\mathbf{d}$ and $\mathbf{I}$ are the superposed diffuse and light source direction matrices, respectively. When the light direction matrix is a full-rank matrix, the surface normal can be obtained as

$$\mathbf{n} = \frac{\mathbf{I}^\dagger \mathbf{d}}{\|\mathbf{I}^\dagger \mathbf{d}\|_2}, \qquad (15)$$

where $\mathbf{I}^\dagger$ is a pseudo-inverse matrix of $\mathbf{I}$.

5. Experiments

The experimental setup is shown in Fig. 6. The target object is illuminated by far infrared spot lights (Exo Terra Heat-Glo 100W) and measured by a thermal camera (InfRec R500). The ambient component is observed before the light source is turned on. Then, the light source is turned on and the change of temperature is captured as a video.

The real light bulb is not stable immediately after turning on and requires a warm-up period in practice. In our experiments, the bulb is warmed up outside the experiment room and brought in under a cover. Removal of the cover is the actual meaning of the light being turned on. The wall
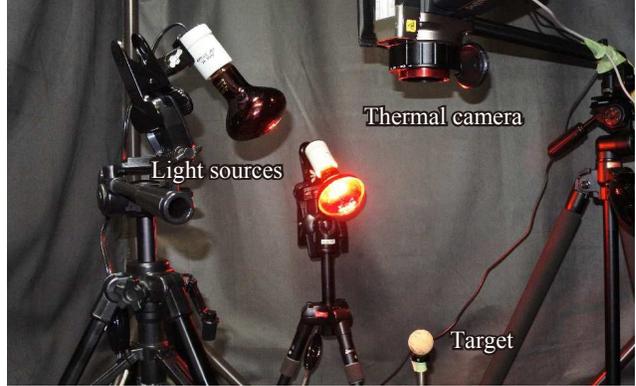
Figure 6: Experimental setup. The object is illuminated by far infrared light and captured by a thermal camera.

of the room is heated over the experiment time and it could become a heat source. To avoid this effect, we place the object far from the wall and the room is actively cooled using an air-conditioner.

Decomposition result A black painted wooden sphere as shown in Fig. 7(a) is measured. A frame of the measured thermal video is shown in Fig. 7(b). Figure 7(c) shows the transition of the measured temperature at the black circular point shown in Fig. 7(b). The ambient component is the measured temperature before turning on the light source, and specular component is the increased intensity immediately after the light source is turned on. The radiation components are the rest, which is shown in Fig. 7(d). The radiation components are not fitted well by a single exponential curve because this is a sum of the diffuse and global radiations. Figure 7(e) shows the decomposed diffuse and global radiations. The sum of these fit well to the observation.

This procedure is applied for all the pixels, and the decomposed images are shown in Figs. 7(f) - (h). The specular component represents the reflection of the light source on the surface, the diffuse radiation represents the reasonable shading, and the global radiation represents the warming of the entire object.

Surface normal estimation By using multiple light source positions and separating each diffuse radiation, we can apply the Lambertian photometric stereo. Figure 8 shows the result of the thermal photometric stereo for the same object as shown in Fig. 7. A normal of the sphere is obtained as shown in Fig. 8(d). The result is compared with the result without light transport decomposition (composition of specular, diffuse, and global) and radiation (composition of diffuse and global) as shown in Fig. 9. As the temperature is not raised around $t = 0$, the compared results are noisy. The error increases owing to the global radiation

(a) The target.　　(b) Example frame.

(c) Temporal profile of the temperature.

(d) Radiation profile.　　(e) Decomposed radiations.

(f) Specular comp.　(g) Diffuse radiation. (h) Global radiation.
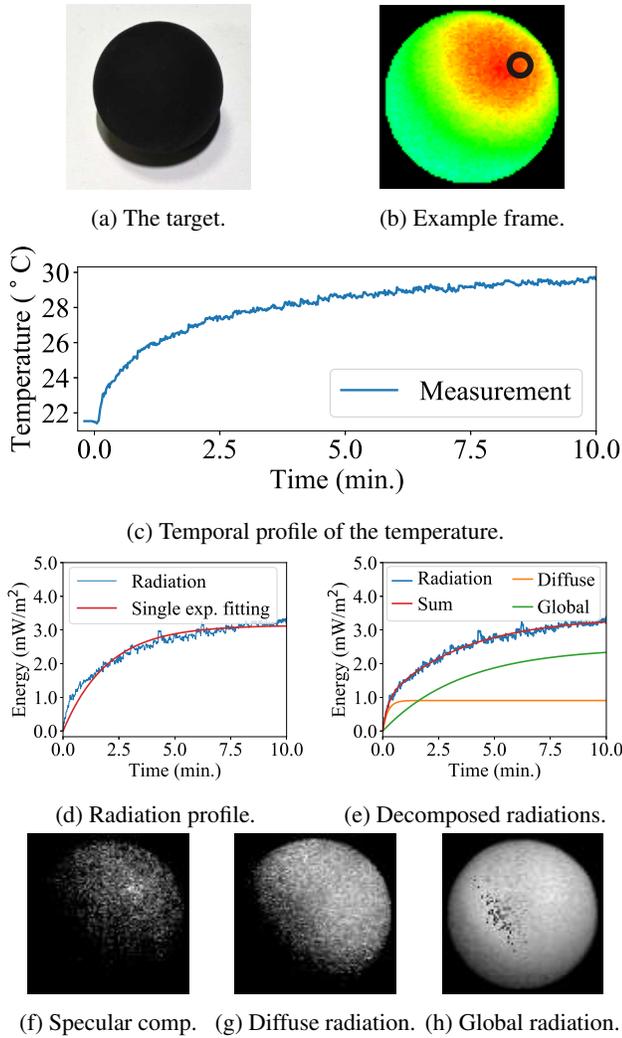
Figure 7: Decomposition result for a black painted wooden ball. (a) The scene. (b) One of thermal video frames. Transient profiles of a point, indicated by the black circle, are shown. (c) Measured temperature transition. (d) Radiation profile. Ambient and specular reflection are subtracted from (c). (e) Decomposed diffuse and global radiations. (f-h) Decomposed images of specular reflection, diffuse, and global radiation, respectively.

at a longer time. As the best result, the angular errors of the result without decomposition and that of radiation is 7.71 and 6.50 degrees, respectively, while our method achieves a better result and the angular error is 5.85 degrees. This result shows the effectiveness of the separation of diffuse radiation.

We apply our method to other materials, including crystal glass, translucent plastic, and translucent marble. The decomposed diffuse component and estimated surface normal are shown in Fig. 10. Because our method is based on

(a)　　(b)　　(c)　　(d)　　(e)
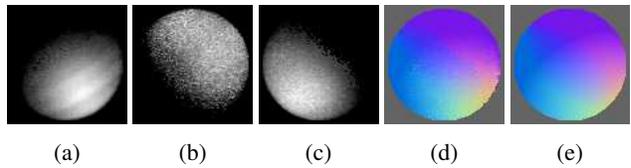
Figure 8: Results of the thermal photometric stereo. (a - c) Decomposed diffuse radiation at different light positions. (d) Estimated surface normal. (e) The ground-truth normal.
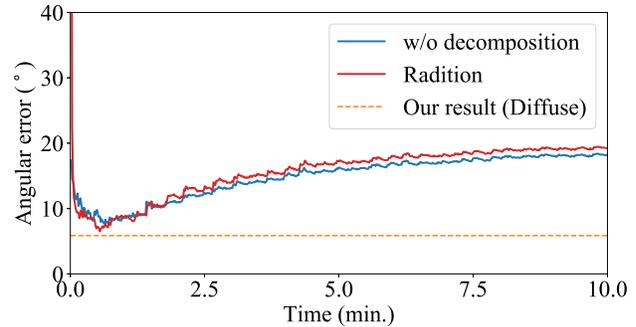
Figure 9: The effectiveness of decomposition. Photometric stereo result without decomposition, result using radiation components, and comparison with our method. Our method is time invariant and the accuracy is shown as a dotted line. The angular error of our method is 5.85 degrees, which shows that our decomposition is effective for the separation of diffuse radiation.

the diffuse radiation, materials that are difficult to measure with the ordinary vision techniques, *e.g.*, transparent and translucent objects, can be measured in the same way. A plastic ornament is also measured, and the result shows the feasibility of our method to a complex shaped objects.

Our method does is not suitable for some objects that does not absorb the far infrared light. Metallic materials are such objects and the thermal observation of a metallic ball is shown in Fig. 11. The metallic ball reflects all the incident light and behaves like a mirror. There is no transient state as shown in Fig. 11(c) which shows there are no radiation components. This problem is identical to the visible light observation.

6. Conclusion

This paper presents a novel technique for the time-resolved decomposition of far infrared light transport. We describe the far infrared light transport model, its transient properties, and that the ordinary vision techniques can be applied to decomposed thermal images. We propose a surface normal reconstruction using a photometric stereo after the diffuse component in a thermal image is separated. Our method recovers the surface normal of any objects that ab-

	The object	Diffuse	Normal

Wood

Crystal glass

Plastic

Marble

Plastic ornament
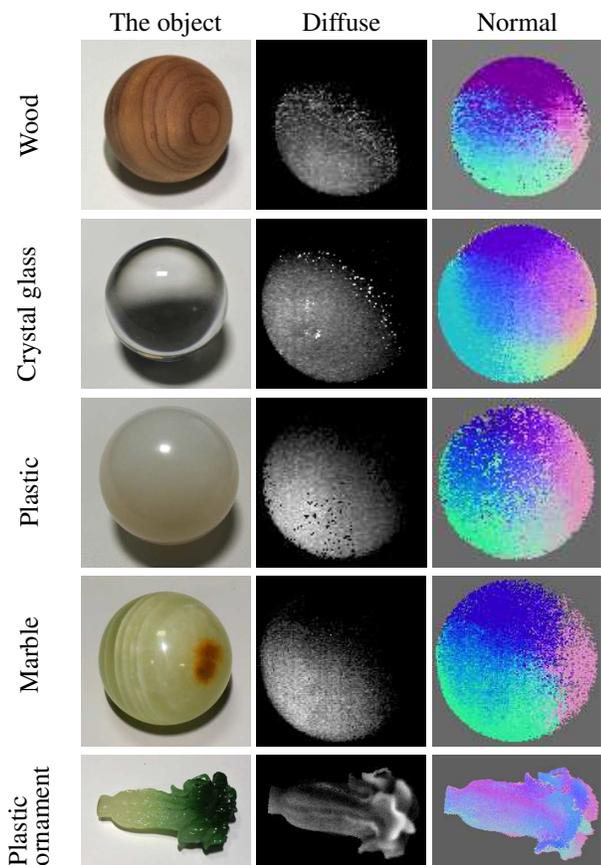
Figure 10: Results on various materials. Spheres made by wood, crystal grass, plastic, and marble are measured, which are challenging objects for ordinary computer vision techniques. Our method uniformly recovers the surface normal for many materials. A complex shape is also measured, and our method recovers the normal appropriately.

(a) Metallic ball.   (b) Observation.   (c) Temperature profile.
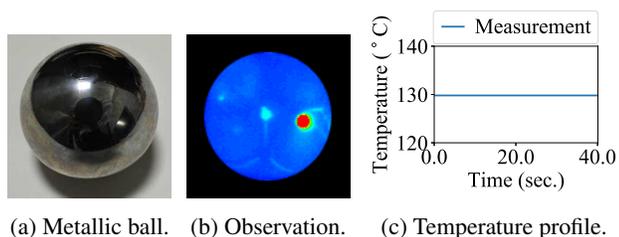
Figure 11: A failure case. The absorption rate is too small hence the metallic ball reflects all the incident light and shows the spherical thermal map of the room. The plot shows the temporal response of the highlighted point, where no transient components are observed. In such a case, only the ambient and specular components can be obtained and the photometric stereo does not work well.

sorbs the incident light, including transparent, translucent, and black objects as well as matte objects.

While the effectiveness of our method is shown by some real-world experiments, some limitations are also encountered. First, the result is noisy owing to the low SNR observations and pixel-wise calculation. Because far infrared light cannot be measured by silicon sensors, the quality of the imaging sensor is not well developed. Naturally, this will be improved in the future, and it will directly improve our results. A global optimization that considers smoothness or simply using a smoothing filter are other options to improve the results.

Another limitation is that some materials, such as metals, do not exhibit much diffuse radiation. In such a case, the ambient and specular components can be separated; however, the photometric stereo is not applicable. This problem is the same as that encountered with visible light observation, *e.g.*, photometric stereo suffers from mirror surface objects. In contrast, the absorption of many objects, including glass, is high, hence the potential applicability of our method is relatively higher than visible light observation techniques.

Acknowledgment

References

[1] A. Bhandari, M. Feigin, S. Izadi, C. Rhemann, M. Schmidt, and R. Raskar. Resolving Multipath Interference in Kinect: an Inverse Problem Approach. In *IEEE SENSORS*, pages 614–617. IEEE, 2014. 2

[2] A. A. Dorrington, J. P. Godbaz, M. J. Cree, A. D. Payne, and L. V. Streeter. Separating True Range Measurements from Multi-Path and Scattering Interference in Commercial Range Cameras. In *SPIE 7864, Three-Dimensional Imaging, Interaction, and Measurement*, page 786404, 2011. 2

[3] G. Eren, O. Aubreton, F. Meriaudeau, L. A. Sanchez Secades, D. Fofi, A. T. Naskali, F. Truchetet, and A. Ercil. Scanning from Heating: 3D Shape Estimation of Transparent Objects from Local Surface Heating. *Optics express*, 17(14):11457–68, 2009. 2

[4] D. Freedman, E. Krupka, Y. Smolin, I. Leichter, and M. Schmidt. SRA: Fast Removal of General Multipath for ToF Sensors. In *Proc. European Conference on Computer Vision (ECCV)*, pages 234–249, 2014. 2

[5] S. Fuchs. Multipath Interference Compensation in Time-of-Flight Camera Images. In *Proc. International Conference on Pattern Recognition*, pages 3583–3586. IEEE, 2010. 2

[6] I. Gkioulekas, A. Levin, F. Durand, and T. Zickler. Micron-Scale Light Transport Decomposition using Interferometry. *ACM Tran. on Graphics (ToG)*, 34(4):37:1–37:14, 2015. 1, 2

[7] J. P. Godbaz, M. J. Cree, and A. A. Dorrington. Closed-Form Inverses for the Mixed Pixel/Multipath Interference Problem in AMCW Lider. In *SPIE 8296, Computational Imaging X*, page 909778, 2012. 2

[8] M. Gupta, S. K. Nayar, M. B. Hullin, and J. Martin. Phasor Imaging: a Generalization of Correlation-Based Time-of-Flight Imaging. *ACM Tran. on Graphics (ToG)*, 34(5):156:1–156:18, 2015. 2

[9] P. Hanrahan and W. Krueger. Reflection from Layered Surfaces Due to Subsurface Scattering. In *Proc. SIGGRAPH*, pages 165–174. ACM Press, 1993. 4

[10] F. Heide, M. B. Hullin, J. Gregson, and W. Heidrich. Low-Budget Transient Imaging using Photonic Mixer Devices. *ACM Tran. on Graphics (ToG)*, 32(4):45:1–45:10, 2013. 1

[11] F. Heide, L. Xiao, W. Heidrich, and M. B. Hullin. Diffuse Mirrors: 3D Reconstruction from Diffuse Indirect Illumination using Inexpensive Time-of-Flight Sensors. In *Proc. Computer Vision and Pattern Recognition (CVPR)*, pages 3222–3229, 2014. 2

[12] F. Heide, L. Xiao, A. Kolb, M. B. Hullin, and W. Heidrich. Imaging in Scattering Media using Correlation Image Sensors and Sparse Convolutional Coding. *Optics express*, 22(21):26338–26350, 2014. 2

[13] J. R. Howell, M. P. Mengüç, and R. Siegel. *Thermal Radiation Heat Transfer, Sixth Edition*. CRC Press, 2015. 3, 4, 6

[14] C. Inoshita, Y. Mukaigawa, Y. Matsushita, and Y. Yagi. Surface Normal Decomposition: Photometric Stereo for Optically Thick Translucent Objects. In *Proc. European Conference on Computer Vision (ECCV)*, pages 346–359, 2014. 2

[15] H. W. Jensen, S. R. Marschner, M. Levoy, and P. Hanrahan. A Practical Model for Subsurface Light Transport. In *Proc. SIGGRAPH*, pages 511–518. ACM Press, 2001. 4

[16] D. Jimenez, D. Pizarro, M. Mazo, and S. Palazuelos. Modelling and Correction of Multipath Interference in Time of Flight Cameras. In *Proc. Computer Vision and Pattern Recognition (CVPR)*, pages 893–900. IEEE, 2012. 2

[17] A. Kadambi, J. Schiel, and R. Raskar. Macroscopic Interferometry: Rethinking Depth Estimation with Frequency-Domain Time-of-Flight. In *Proc. Computer Vision and Pattern Recognition (CVPR)*, pages 893–902, 2016. 2

[18] A. Kadambi, H. Zhao, B. Shi, and R. Raskar. Occluded Imaging with Time-of-Flight Sensors. *ACM Tran. on Graphics (ToG)*, 35(2):15:1–15:12, 2016. 2

[19] A. Kirmani, A. Benedetti, and P. A. Chou. SPUMIC: Simultaneous Phase Unwrapping and Multipath Interference Cancellation in Time-of-Flight Cameras using Spectral Methods. In *IEEE International Conference on Multimedia and Expo (ICME)*, pages 1–6. IEEE, 2013. 2

[20] K. Kitano, T. Okamoto, K. Tanaka, T. Aoto, H. Kubo, T. Funatomi, and Y. Mukaigawa. Recovering Temporal PSF using ToF Camera with Delayed Light Emission. *IPSJ Trans. on Computer Vision and Applications*, 9(15), June 2017. 1

[21] B. Lamond, P. Peers, and P. Debevec. Fast Image-Based Separation of Diffuse and Specular Reflections. In *Proc. SIGGRAPH Sketches*, page 74, 2007. 2

[22] S. Lee and H. Shim. Skewed Stereo Time-of-Flight Camera for Translucent Object Imaging. *Image and Vision Computing*, 43(C):27–38, 2015. 2

[23] D. Miyazaki, M. Saito, Y. Sato, and K. Ikeuchi. Determining surface orientations of transparent objects based on polarization degrees in visible and infrared wavelengths. *Journal of the Optical Society of America A*, 19(4):687–694, 2002. 2, 4

[24] Y. Mukaigawa, R. Raskar, and Y. Yagi. Analysis of Light Transport in Scattering Media. In *Proc. Computer Vision and Pattern Recognition (CVPR)*, pages 153–160, 2010. 2

[25] Z. Murez, T. Treibitz, R. Ramamoorthi, and D. J. Kriegman. Photometric Stereo in a Scattering Medium. *IEEE Transactions on Pattern Analysis and Machine Intelligence*, 39(9):1880–1891, Sept 2017. 2

[26] N. Naik, A. Kadambi, C. Rhemann, S. Izadi, R. Raskar, and S. Bing Kang. A Light Transport Model for Mitigating Multipath Interference in Time-of-Flight Sensors. In *Proc. Computer Vision and Pattern Recognition (CVPR)*, pages 73–81, 2015. 2

[27] N. Naik, S. Zhao, A. Velten, R. Raskar, and K. Bala. Single View Reflectance Capture using Multiplexed Scattering and Time-of-Flight Imaging. *ACM Tran. on Graphics (ToG)*, 30(6):171:1–171:10, 2011. 2

[28] S. K. Nayar, X.-S. Fang, and T. Boult. Separation of Reflection Components Using Color and Polarization. *International Journal of Computer Vision (IJCV)*, 21(3):163–186, 1997. 2

[29] S. K. Nayar, G. Krishnan, M. D. Grossberg, and R. Raskar. Fast Separation of Direct and Global Components of a Scene using High Frequency Illumination. *ACM Tran. on Graphics (ToG)*, 25(3):935–944, 2006. 1, 2

[30] T. T. Ngo, H. Nagahara, and R. Taniguchi. Shape and Light Directions from Shading and Polarization. In *Proc. Computer Vision and Pattern Recognition (CVPR)*, 2015. 2

[31] T. Nguyen, Q. N. Vo, H.-J. Yang, S.-H. Kim, and G.-S. Lee. Separation of specular and diffuse components using tensor voting in color images. *Applied optics*, 53(33):7924–7936, 2014. 2

[32] M. O'Toole, S. Achar, S. G. Narasimhan, and K. N. Kutulakos. Homogeneous Codes for Energy-Efficient Illumination and Imaging. *ACM Tran. on Graphics (ToG)*, 34(4):35:1–35:13, 2015. 2

[33] M. O'Toole, F. Heide, L. Xiao, M. B. Hullin, W. Heidrich, and K. N. Kutulakos. Temporal Frequency Probing for 5D Transient Analysis of Global Light Transport. *ACM Tran. on Graphics (ToG)*, 33(4):87:1–87:11, 2014. 2

[34] M. O'Toole, J. Mather, and K. N. Kutulakos. 3D Shape and Indirect Appearance by Structured Light Transport. In *Proc. Computer Vision and Pattern Recognition (CVPR)*, pages 3246–3253. IEEE, 2014. 2

[35] M. O'Toole, R. Raskar, and K. N. Kutulakos. Primal-Dual Coding to Probe Light Transport. *ACM Tran. on Graphics (ToG)*, 31(4):39:1–39:11, 2012. 2

[36] M. O'Toole, F. Heide, D. Lindell, K. Zang, S. Diamond, and G. Wetzstein. Reconstructing Transient Images from Single-Photon Sensors. In *Proc. Computer Vision and Pattern Recognition (CVPR)*, 2017. 1

[37] H. Qiao, J. Lin, Y. Liu, M. B. Hullin, and Q. Dai. Resolving Transient Time Profile in ToF Imaging via Log-Sum Sparse Regularization. *Optics letters*, 40(6):918–21, 2015. 2

[38] W. Ren, J. Tian, and Y. Tang. Specular Reflection Separation With Color-Lines Constraint. *IEEE Trans. on Image Processing*, 26(5):2327–2337, 2017. 2

[39] P. Saponaro, S. Sorensen, A. Kolagunda, and C. Kambhamettu. Material Classification with Thermal Imagery. In *Proc. Computer Vision and Pattern Recognition (CVPR)*, pages 4649–4656, 2015. 2

[40] Y. Sato and K. Ikeuchi. Temporal-color Space Analysis of Reflection. *Journal of the Optical Society of America A*, 11(7):2990–3002, 1994. 2

[41] S. A. Shafer. Using Color to Separate Reflection Components. *Color Research & Application*, 10(4):210–218, 1985. 1, 2

[42] H. Shim and S. Lee. Recovering Translucent Object using a Single Time-of-Flight Depth Camera. *IEEE Transactions on Circuits and Systems for Video Technology*, 26(5):841–854, 2015. 2

[43] K. Tanaka, Y. Mukaigawa, H. Kubo, Y. Matsushita, and Y. Yagi. Recovering Transparent Shape from Time-of-Flight Distortion. In *Proc. Computer Vision and Pattern Recognition (CVPR)*, pages 4387–4395, 2016. 2

[44] K. Tanaka, Y. Mukaigawa, H. Kubo, Y. Matsushita, and Y. Yagi. Recovering Inner Slices of Layered Translucent Objects by Multi-frequency Illumination. *IEEE Trans. on Pattern Analysis and Machine Intelligence (TPAMI)*, 39(4):746–757, 4 2017. 4

[45] K. Tanaka, Y. Mukaigawa, Y. Matsushita, and Y. Yagi. Descattering of Transmissive Observation using Parallel High-Frequency Illumination. In *Proc. International Conference on Computational Photography (ICCP)*, pages 96–103. IEEE, 2013. 2

[46] T. Treibitz, Z. Murez, B. G. Mitchell, and D. Kreigman. Shape from Fluorescence. In *Proc. European Conference on Computer Vision (ECCV)*, 2012. 2

[47] T. Treibitz and Y. Y. Schechner. Active Polarization Descattering. *IEEE Trans. on Pattern Analysis and Machine Intelligence (TPAMI)*, 31(3):385–399, 2009. 1, 2

[48] C.-Y. Tsai, K. N. Kutulakos, S. G. Narasimhan, and A. C. Sankaranarayanan. The Geometry of First-Returning Photons for Non-Line-Of-Sight Imaging. In *Proc. Computer Vision and Pattern Recognition (CVPR)*, 2017. 2

[49] A. Velten, R. Raskar, D. Wu, A. Jarabo, B. Masia, C. Barsi, C. Joshi, E. Lawson, M. Bawendi, and D. Gutierrez. Femto-Photography: Capturing and Visualizing the Propagation of Light. *ACM Tran. on Graphics (ToG)*, 32(4):44:1–44:8, 2013. 4

[50] L. B. Wolff and T. E. Boult. Constraining Object Features using a Polarization Reflectance Model. *IEEE Trans. on Pattern Analysis and Machine Intelligence (TPAMI)*, 13(7):635–657, 1991. 2

[51] R. J. Woodham. Photometric method for determining surface orientation from multiple images. *Optical Engineering*, 19(1):139–144, 1980. 2

[52] D. Wu, A. Velten, M. O'Toole, B. Masia, A. Agrawal, Q. Dai, and R. Raskar. Decomposing Global Light Transport using Time of Flight Imaging. *International Journal of Computer Vision (IJCV)*, 107(2):123–138, 2014. 1, 2